PHYSICAL REVIEW B **87**, 024424 (2013)

Crossover in the surface anisotropy contributions of ferromagnetic films on rippled Si surfaces

M. O. Liedke,[1,*] M. Körner,[1,2] K. Lenz,[1] M. Fritzsche,[1,2] M. Ranjan,[1,†] A. Keller,[1] E. Čižmár,[3,‡] S. A. Zvyagin,[3] S. Facsko,[1]
K. Potzger,[1] J. Lindner,[1] and J. Fassbender[1,2]

[1]*Institute of Ion Beam Physics and Materials Research, Helmholtz-Zentrum Dresden-Rossendorf, P.O. Box 510119, 01314 Dresden, Germany*
[2]*Technical University Dresden, Helmholtzstr. 10, 01609 Dresden, Germany*
[3]*Dresden High Magnetic Field Laboratory (HLD), Helmholtz-Zentrum Dresden-Rossendorf, P.O. Box 510119, 01314 Dresden, Germany*

(Received 26 June 2012; published 31 January 2013)

We investigate the influence of a nanoscale periodic ripple morphology on the structure and magnetocrystalline anisotropy of thin ferromagnetic (FM) $Ni_{81}Fe_{19}$, Co, and Fe films. The ripples are created by ion beam erosion of the Si substrate. The periodic ripple structures induce a uniaxial magnetic anisotropy (UMA) in the FM films as confirmed by ferromagnetic resonance and magneto-optical Kerr effect measurements. The thickness dependence of the UMA reveals an abrupt transition. For a thin film regime there is a corrugated alignment of the magnetic moments and above a critical thickness one has dipolar interactions due to the sinusoidal surface modulations.

DOI: 10.1103/PhysRevB.87.024424 PACS number(s): 75.75.−c, 75.30.Gw, 81.16.Rf, 76.50.+g

I. INTRODUCTION

It is well established that ion beam erosion (IBE) processes can be utilized for the modification of the surface morphology.[1] Typically, due to ion irradiation either a surface smoothening or stochastic roughening is achieved that, under controlled irradiation conditions, can evolve into self-organized periodic patterns, e.g. dots, cones, or ripples.[2–4] The versatility of this approach to surface modification originates from only several irradiation parameters, like ion species, ion energy, angle of incidence, ion flux, and temperature of the surface. Moreover, basically most material classes, e.g., semiconductors, metals, and insulators, can be or have been utilized for surface morphology modification leading to similar surface profiles.[3]

First experiments associated with modifications of the surface morphology due to IBE processes, where ripple profiles were created, were performed in the 1960s by Navez *et al.*[5] The first theoretical predictions for the mechanism of ripple formation were proposed by Bradley and Harper (BH)[6] based on Sigmund's theory of sputtering.[7] According to this theory the ripple formation originates from the competition of two counteracting processes: (i) the curvature dependent ion induced surface instability that grows faster for the surface trough than for the crest, and (ii) the diffusion, which tends to smoothen the surface. Thus, due to the larger power deposited by incoming ions at the trough's surface, a larger erosion rate is expected there compared to that on the crests. At the same time, diffusion stabilizes the overall surface morphology to the shape of a wave. Further detailed explanations of the overall ripple formation process can be found elsewhere.[4,8]

The BH model gives a general and simplified view into the ion induced surface morphology modification processes. However, it assumes an exponential growth of the ripple amplitude with time and a constant ripple wavelength, which is inconsistent with some experimental observations, e.g., the nonexponential evolution of the ripple amplitude followed by saturation, wavelength coarsening, and fluence-dependent ripple rotation. Despite amorphous materials or semiconductors, where the BH model gives acceptable agreement, more sophisticated models have been developed to account for these inconsistencies.[3,9]

In recent studies involving IBE processes focused on the modification of magnetic properties, several material classes were of interest: (i) irradiation of single-crystalline magnetic materials, like Fe[10,11] or Co,[12,13] (ii) irradiation of polycrystalline magnetic materials, e.g., Fe and Ni,[14,15] and (iii) irradiation of planar templates followed by a deposition of magnetic materials.[16–20] Among these three approaches, IBE of single-crystalline films represents the most complex magnetic behavior, where despite the intrinsic cubic magnetic anisotropy an additional in-plane uniaxial contribution is superimposed due to the ripple morphology. The origin of the uniaxial magnetic anisotropy (UMA) in these systems has been related to the spin-orbit coupling modification, i.e., to the symmetry breaking at the monoatomic steps of the ripple slope, like for magnetic thin films grown on vicinal surfaces.[21,22] Moreover, it was shown that a distribution of monoatomic steps plays a crucial role for the UMA strength and strongly increases with the ion fluence.[10,11,13] In the case of irradiation of polycrystalline magnetic materials as well as for the deposition of polycrystalline magnetic materials on prepatterned templates, the UMA is dominant since the orientation of individual grains in these systems is random and no preferred step orientation can be selected. Thus, the origin of UMA here can be different than for single-crystal patterned films and is strictly related to magnetostatic contributions of the overall magnetic anisotropy, e.g., shape anisotropy and dipolar interactions.[14–19] Due to the induced UMA, rippled films have been suggested for application in magnetic sensors.[23,24] Additional UMA contributions are known to exist as well, for example in single-crystal systems, where spontaneous pattern formation during epitaxial growth takes place[25,26] or can be induced by oblique metal deposition with respect to the sample plane.[27]

In two of our previous studies[16,17] we have demonstrated that a ripple formation, e.g., due to dipolar effects, gives rise to an increase of the uniaxial magnetic anisotropy in the exchange bias $Ni_{81}Fe_{19}/Fe_{50}Mn_{50}$ system[16] and modifies a Néel type interlayer exchange coupling in thin polycrystalline Fe/Cr/Fe trilayers.[17]

In this paper we will demonstrate the evolution of magnetic anisotropy as a function of the ripple template wavelength λ for $3d$ ferromagnets of constant thickness of 10 nm, namely Permalloy ($Py = Ni_{81}Fe_{19}$), Co, and Fe, deposited by molecular beam epitaxy (MBE) on rippled Si/SiO_2 substrates.

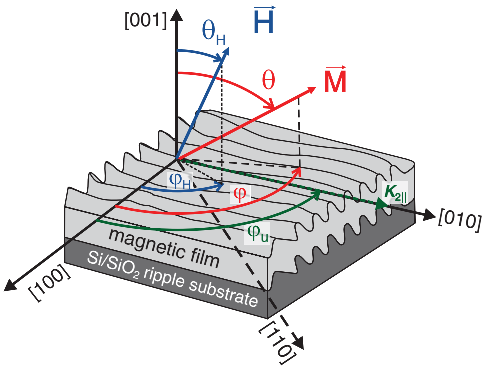

FIG. 1. (Color online) Schematic picture of the sample with the coordinate system for the magnetic measurements.

The main result of these studies is the generation of a large UMA ($K_{2\|}$) originating from the periodic modulation of the interfaces. Moreover, based on thickness-dependent investigations of all aforementioned metals, we will unambiguously show that the UMA scales and originates from dipolar interaction, i.e., stray fields created by the curvature.

In Sec. II the details of the sample preparation, their structure, and experimental details are presented, followed by the results and discussion in Sec. III. In Sec. IV the conclusion is given.

II. EXPERIMENTAL DETAILS

In order to obtain nanoripple templates commercially available single-side polished Si(100) 1×1 cm^2 substrates have been used. The substrates have been irradiated by Ar$^+$ or Xe$^+$ ions in the energy range of 0.3–15 keV at an incident angle of 67° with respect to the surface normal and at a constant ion fluence from a range of $0.2–2 \times 10^{18}$ ions/cm^2, allowing fabrication of self-organized ripple templates with a wavelength range of 25–90 nm and an average amplitude range of 1.5–5 nm. Details of the sputtering process are reported elsewhere.[28,29] Subsequently, the three polycrystalline ferromagnetic materials Py, Fe, and Co have been deposited onto the nanoripple templates by means of MBE: (I) as continuous 10 nm thick films onto several templates with modulation wavelengths of 25, 35, 47, 70, and 88 nm, and (II) as wedges with thickness gradients of 0–50 nm onto 25 nm ripple templates. All samples have been capped by a 2 nm thick Cr protective layer. The film thickness was monitored *in situ* by a calibrated quartz crystal microbalance. The base and evaporation pressure in the ultrahigh vacuum chamber was about 1×10^{-10} and $\leqslant 8 \times 10^{-9}$ mbar, respectively. Evaporation was performed under normal incidence, at room temperature with a deposition rate of $\approx$0.2 Å/s. Figure 1 shows a sketch of the type-I samples with the coordinate system for the magnetic measurements.

Prior and after deposition of the metal films, the surface topography was checked by atomic force microscopy (AFM). The image processing was performed using the WSxM software.[30] Magnetic properties analysis was determined by means of scanning longitudinal magneto-optical Kerr effect (MOKE), vector network analyzer ferromagnetic resonance (VNA-FMR), and X-band FMR magnetometry.

III. RESULTS AND DISCUSSION

A. Atomic force microscopy

In Fig. 2 AFM micrographs of the Si nanoripple templates are shown. AFM scans were fast Fourier transformed (FFT) in order to extract information about the roughness distribution, i.e., the ripple wavelength (see the insets of each scan). These 2D power spectrum density (PSD) distributions consist usually of a center peak and two satellite peaks due to the anisotropic and periodical nature of the ripple patterns. The ripple wavelength λ was determined as the distance between satellite peaks and is denoted below each PSD. The lowest λ achieved and used in our experiments was about 25 nm, the largest about 90 nm. Overall, the vertical elongation of the satellite peaks in the PSD spectra corresponds to the fact that the ripples are not perfectly straight but rather exhibit some curved features, which is also visible in all the images. On the other hand, for ripple wavelengths of $\lambda = 35$ and 47 nm the PSD spectra of Figs. 2(b) and 2(c) show that both the central and satellite peaks are more rounded than vertically elongated, and broad that suggests that the ripple alignment along their crests is better than for the rest of the samples. The other important parameter, the short range ordering, can be assessed as the relation between the ripple wavelength λ and the correlation length ξ that is the inverse full width at half maximum (FWHM) value of the first order satellite peak measured in the perpendicular direction to the ripple crests, namely ξ/λ. The correlation length ξ describes the lateral ordering of structures on the surface, and it indicates the length scale of the correlation, e.g., the average domain size.[31] The short range ordering ξ/λ is found to increase steadily with the ripple wavelength λ as well as the ion energy (see Table I). The root mean square (rms) roughness $\omega_{\rm rms}$ and ripple amplitude δ follow roughly a linear dependence as a function of ion energy (not shown).[4] Moreover, the aspect ratio between the ripple amplitude δ and the ripple wavelength λ is typically smaller than about 1:20. In Table I the calculated values of $\omega_{\rm rms}$, δ, and ξ/λ for all

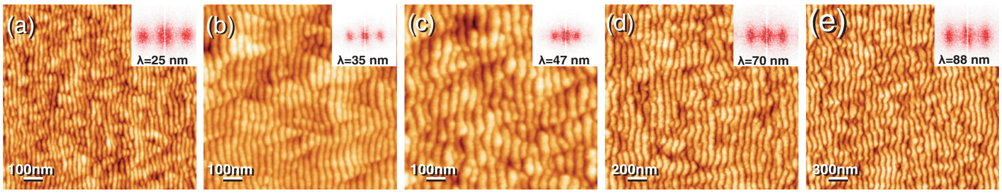

FIG. 2. (Color online) AFM scans of the Si nanoripple templates for different ripple wavelengths. Insets show the corresponding PSD spectra.

TABLE I. Morphological details of the templates acquired from the AFM measurements.

Ripple wavelength λ (nm)	rms ω_{rms} (nm)	Ripple amplitude δ (nm)	Order parameter ξ/λ
25	1.15	2.3	2.22
35	1.16	2.4	3.17
47	1.20	2.6	3.22
70	1.28	3.5	3.57
88	1.80	4.4	5.55

ripple templates are listed. In comparison to a commercial Si substrate ω_{rms} is about one order of magnitude larger. After the deposition of magnetic metals the ripple wavelength remained constant, whereas ω_{rms} and δ are slightly increased by less than 10%.

B. Magneto-optical Kerr effect measurements

The magnetic characterization of the samples was performed in a first step by MOKE measurements. Angular in-plane dependencies for all the magnetic materials and ripple wavelengths were taken at 1° steps over a 360° circle. The magnetization reversal (MR) curves were analyzed with respect to the remanence M_{r} and coercive field H_{c}. Figure 3(a) shows M_{r} as a function of the in-plane magnetic field angle φ_{H} for Py films with different ripple wavelengths including a planar substrate. One can clearly see that in all cases M_{r} exhibits a regular figure-eight shape, which indicates a strong uniaxial magnetic anisotropy present in the system. Despite the fact that the sample with Py was evaporated on the planar substrate, the maximum of M_{r}, i.e., the easy magnetization axis, coincides with a direction parallel to the ripple crests, i.e., $\phi_{\mathrm{ripple}} = 90^\circ$. In the case of the planar Py sample the easy magnetization direction is aligned along a residual magnetic field orientation that was present during deposition (a few Oersted large). For all ripple wavelengths a similar behavior for the three magnetic materials was observed in the $M_{\mathrm{r}}(\varphi_{\mathrm{H}})$ angular dependence (only the Py case is shown).

The angular dependence of H_{c} is more complicated, therefore it needs to be discussed for each magnetic metal separately. Among the three magnetic metals investigated, Py, due to its soft magnetic properties, represents the sharpest coercivity distribution [cf. Fig. 3(b)]. For Co [Fig. 3(c)] and Fe [Fig. 3(d)] that are considered as hard magnetic materials compared to Py, and where the magnetocrystalline anisotropy contributions play a larger role, the distribution of H_{c} is much broader and of a different symmetry. In all the cases the distribution of H_{c} has a minimum surrounded by two sharp maxima for the direction perpendicular to the ripple crest direction (hard axis), and an additional broad maximum in the parallel orientation (easy axis). For the Py and Co samples the largest H_{c} values are found for $\lambda = 35$ nm, whereas for Fe samples the largest H_{c} of 90 Oe is obtained for the smallest ripple wavelength ($\lambda = 25$ nm). In general, after H_{c} peaks, it decreases as function of λ for all three materials. In other words M_{r} and H_{c} distributions clearly show a strong uniaxial behavior due to the ripple modulation that scales down with the ripple wavelength.

C. Ferromagnetic resonance

The ferromagnetic resonance investigations were carried in a conventional, cavity based X-band setup (X-band Bruker Elexsys E500 spectrometer equipped with a goniometer) and a broadband vector network analyzer (VNA) setup, latter in field-sweep mode, i.e., keeping the microwave frequency fixed at $\omega/2\pi = 9.38$ GHz while sweeping the external magnetic field H. All the measurements have been performed at room temperature. The samples were mounted inside the cavity and/or on the center of a coplanar waveguide attached to the VNA's ports, respectively. For the VNA analysis the microwave transmission parameter S_{21} was recorded as the FMR signal. The FMR spectra taken at different in-plane field angles φ_H were evaluated using the real part of the complex Lorentzian L:

$$\mathrm{Re}(L) = \frac{A\Delta R[\Delta R\cos\phi + (H - H_{\mathrm{res}})\sin\phi]}{(\Delta R)^2 + (H - H_{\mathrm{res}})^2}, \tag{1}$$

where A is the amplitude of the signal and ϕ is a phase factor to handle the frequency dependent mixture of absorption and dispersion of the broadband setup. The linewidth ΔR can be expressed in the notation of a classic Lorentz absorption derivative peak-to-peak linewidth (cavity-based FMR) by $\Delta H_{\mathrm{pp}} = 2\Delta R/\sqrt{3}$.

From the resulting angular dependencies of the resonance field data $H_{\mathrm{res}}(\varphi_H)$ the magnetic anisotropy parameters were

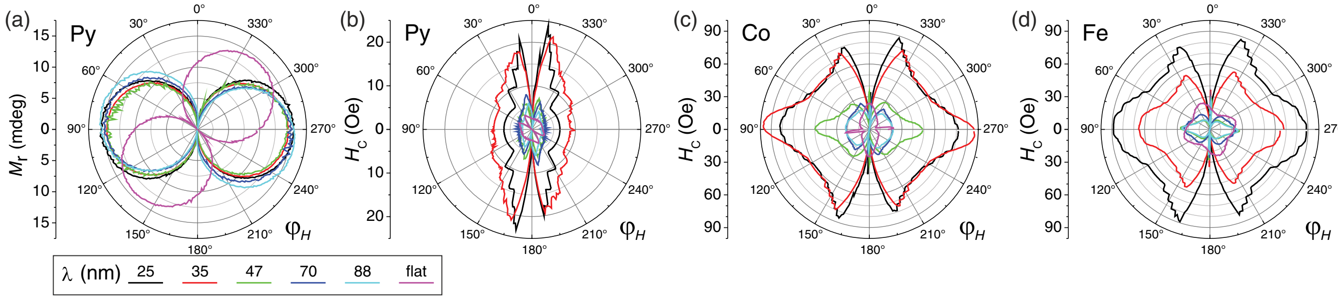

FIG. 3. (Color online) Angle-dependent MOKE scans of (a) the Py remanence M_{r}. (b)–(d) The coercive fields H_{c} of Py, Co, and Fe for different ripple wavelengths and for a planar reference substrate, respectively.

determined by fitting the resonance equation

$$\begin{aligned}\left(\frac{\omega}{\gamma}\right)^2 = {} & \left[H_{\mathrm{res}}\cos(\varphi-\varphi_H)+\frac{2K_{2\parallel}}{M}\cos 2(\varphi-\varphi_u)\right.\\ & \left.+\frac{2K_{4\parallel}}{M}\cos 4\varphi\right]\\ & \times\left[H_{\mathrm{res}}\cos(\varphi-\varphi_H)+4\pi M_{\mathrm{eff}}+\frac{2K_{2\parallel}}{M}\cos^2(\varphi-\varphi_{\mathrm{u}})\right.\\ & \left.+\frac{K_{4\parallel}}{2M}(3+\cos 4\varphi)\right]\end{aligned} \tag{2}$$

to the data. γ denotes the gyromagnetic ratio, φ is the in-plane angle of the magnetization M. $K_{4\parallel}$ is the magnetocrystalline cubic anisotropy and $K_{2\parallel}$ is the uniaxial in-plane anisotropy. The effective magnetization is defined as the difference between the demagnetizing field and the perpendicular uniaxial anisotropy field: $4\pi M_{\mathrm{eff}} := 4\pi M - 2K_{2\perp}/M$. The uniaxial in-plane anisotropy direction with respect to the cubic direction is denoted by φ_{u}. All in-plane angles φ,φ_H, and φ_{u} are counted from the [100] direction, as depicted in Fig. 1. Equation (2) is derived using the free energy density:

$$\begin{aligned}F = {} & -MH\,[\sin\theta\sin\theta_H\cos(\varphi-\varphi_H)+\cos\theta\cos\theta_H]\\ & -(2\pi M^2-K_{2\perp})\sin^2\theta - K_{2\parallel}\sin^2\theta\cos^2(\varphi-\varphi_{\mathrm{u}})\\ & -\tfrac{1}{8}K_{4\parallel}\,(3+\cos 4\varphi)\sin^4\theta,\end{aligned} \tag{3}$$

where θ (θ_H) is the polar angle of M (H), respectively. θ_H is set to 90° since all the measurements are performed in-plane.

Figures 4(a)–4(c) show the angular dependencies of the resonance field $H_{\mathrm{res}}(\varphi_H)$ for the three materials Py [Fig. 4(a)], Co [Fig. 4(b)], and Fe [Fig. 4(c)] for different ripple wavelengths. The solid lines are fits according to the resonance equation (2). All samples have been measured by X-band FMR or VNA-FMR. All data sets show a pronounced minimum at $\varphi_H = 90°$ and maxima at 0° and 180° clearly indicating the existence of strong UMA. The minimum position corresponds to the easy axis orientation, i.e., along ripple crests, as also determined by MOKE.

The "amplitude" of the fit curve is proportional to the in-plane uniaxial anisotropy field. For all three metals this amplitude and thus the uniaxial anisotropy decreases monotonically with increasing λ in a very similar manner. This dependence is clearly depicted in Fig. 5(a) where the uniaxial in-plane anisotropy field $2K_{2\parallel}/M$ is plotted against λ. In the low wavelength regime (λ = 20–50 nm) the UMA field has a strong dependence on λ. For larger λ (above 50 nm) the UMA field decreases only slightly saturating at a residual UMA of around $2K_{2\parallel}/M \approx 20$ Oe for the planar samples. Furthermore, the saturation field H_{s} that is an equivalent measure of the UMA, obtained from the hard-axis MOKE measurements is in agreement with the FMR analysis $2K_{2\parallel}/M$ as depicted in Fig. 5(a). There is a systematic offset of H_{s} with respect to $2K_{2\parallel}/M$ which is due to the fact that the saturation field H_{s} was taken from the point where the hysteresis curve reaches its saturation. This overestimates the true uniaxial anisotropy especially if there are other small anisotropy contributions involved that lead to the small curved tail close to saturation. We have found this constant offset as well for 2.5 nm thin films (not shown).

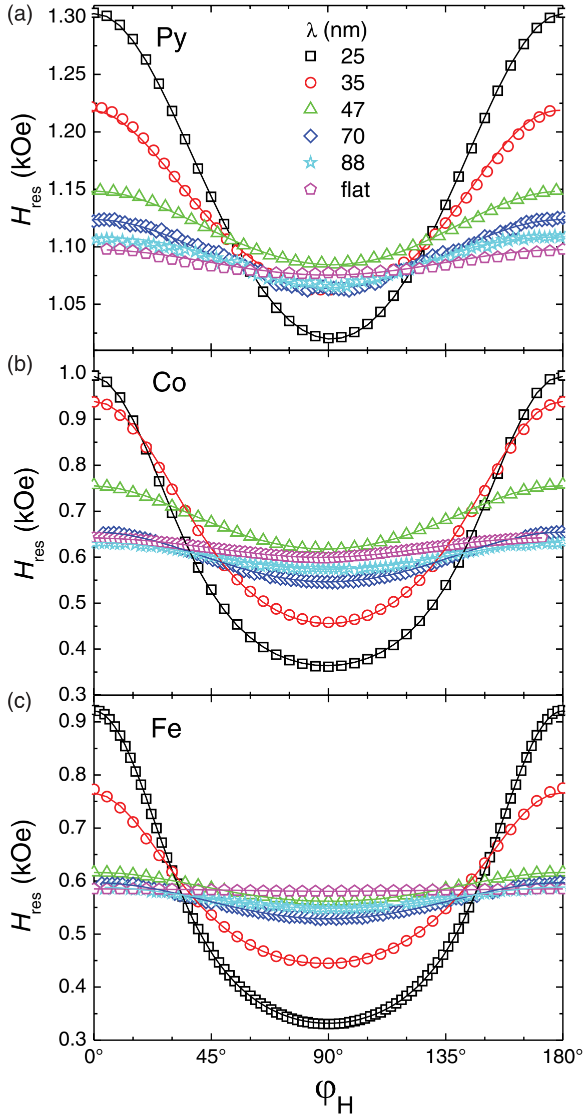

FIG. 4. (Color online) Angular dependence of the resonance fields H_{res} for (a) Py, (b) Co, and (c) Fe samples for different ripple wavelengths. Solid lines are fits according to the resonance equation (2). Measurements have been done at room temperature.

The effective magnetization $4\pi M_{\mathrm{eff}}$ as shown in Fig. 5(b) is more or less constant for all three metals irrespective to the ripple wavelength. However the values are ≈18% smaller compared to the bulk literature values ($4\pi M_{\mathrm{s}} \approx 10.08$, 17.6, 21.3, for Py, Co, Fe, respectively). Since FMR measures the effective out-of-plane anisotropy field the saturation magnetization M_{s} cannot be derived directly. The fact that the effective anisotropy field is smaller than $4\pi M_{\mathrm{s}}$ might be related to an easy out-of-plane anisotropy that results from film texture. This is known to occur for hexagonally closely packed (hcp) Co films, where the strong (0001) texture determines the easy crystallographic axis, thus reducing the effective magnetization M_{eff}.[32] Our measurements by FMR and superconducting quantum interference device magnetometry (SQUID) yield a $4\pi M_{\mathrm{eff}}$ of about 13.5 kG compared to $4\pi M_{\mathrm{s}} \approx 17$ kG. Thus,

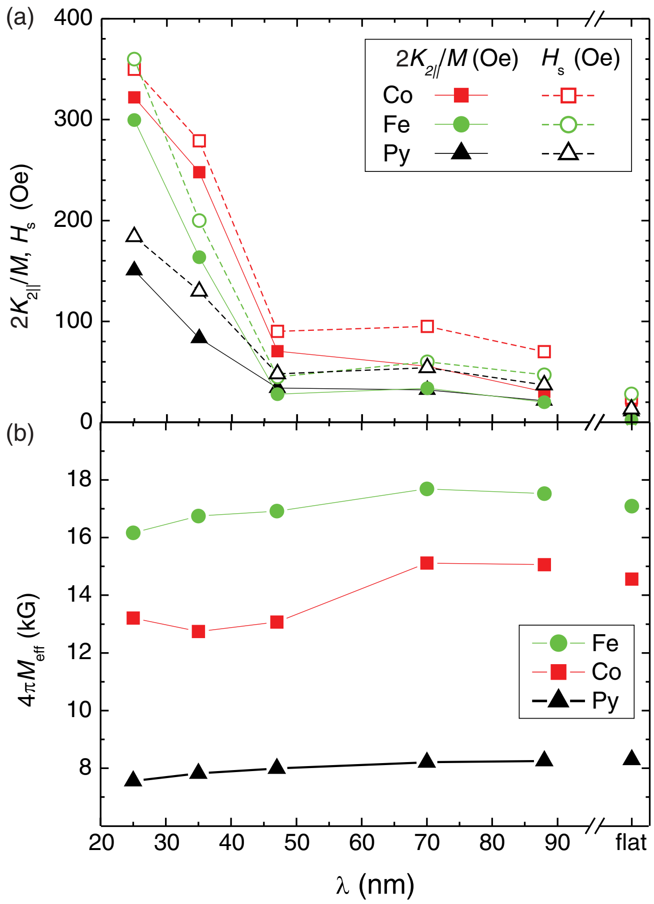

FIG. 5. (Color online) Ripple wavelength dependence of (a) the uniaxial in-plane anisotropy field (solid symbols) and MOKE saturation field (open symbols), as well as (b) the effective magnetization. Lines are guides to the eye only.

this is indeed the case here, where despite the lower $4\pi M_{\text{eff}}$ the saturation magnetization M_s is almost bulklike. For Fe the texture effect is typically less pronounced as its crystalline anisotropy is cubic (not uniaxial as for Co) and thus much smaller. The strong reduction of $4\pi M_{\text{eff}}$ for Fe compared to the bulk M_s cannot be explained purely by texture, thus indeed M_s must be smaller. Our SQUID measurements indicate a value of $4\pi M_s \approx 15$ kG.

The decrease of UMA with the template periodicity suggests a strong decay of dipolar interactions with increasing ripple wavelength. In order to obtain perfect fits [solid lines in Figs. 4(a)–4(c)] a small cubic anisotropy field $2K_{4\|}/M$ had to be added to the overall anisotropy for Fe and Co. However, the $2K_{4\|}/M$ values are about two orders of magnitude smaller than $2K_{2\|}/M$, hence, negligible.

As mentioned above, Fe and Co even in their polycrystalline form still exhibit intrinsically a cubic anisotropy mainly due to the material's texture. Nevertheless, the randomness of the crystallographic orientations in the polycrystalline grains helps to understand the origins of the ripple-induced UMA. Only a few reasons will be considered here: (i) monoatomic steps, (ii) strain, or (iii) shape. The first two can be ruled out immediately due to the random orientation in polycrystalline systems, i.e., monoatomic step orientations will average out. The strain is eased by the convex surface morphology, respectively. The most favorable origin of UMA would be the shape related contributions, e.g., dipolar interaction throughout ripple crests. Thus, due to the generation of stray fields across the ripple crests, the free energy density function is largest compared to the parallel orientation, where it is lowest. This corresponds to the hard (perpendicular to ripple crests) and easy axis orientations (parallel to ripple crests) of the magnetization, respectively.

We will discuss the wavelength range in detail where the dipolar interaction plays a role and its relation to the ripple induced UMA in the next sections. Before that, it is important to notice that the cause for the quite low Fe UMA value (compared to the larger Co value) is somehow unclear [see Fig. 5(a)]. From simple arguments, just taking dipolar effects into account, one would expect a higher UMA for the film with higher magnetic moment, i.e., Fe. Possible origins for the observed discrepancy are likely due to magnetostrictive interactions, which were not taken into account so far.

D. UMA thickness dependence

In order to investigate the relevance of the dipolar interactions with respect to the ripple induced UMA, the wedge-type series II of samples was used, where the film's thickness t was varied in the range of 0–50 nm. For this particular experiment a ripple wavelength of $\lambda = 25$ nm was used, because the largest UMA field was achieved in this system.

In Fig. 6 for each material three magnetization reversal (MR) curves measured by MOKE are shown. The magnetic field was applied in the hard direction, i.e., perpendicular to the ripple crests in the [100] direction. The curves were taken at three distinguished spots along the metal wedge representing different thicknesses. Corresponding AFM images were taken from the same regions. By this the relation between the magnetic response of the system compared to the sample topography, roughness, and template coverage can be investigated. The morphological correlation lengths and ordering are analyzed in more detail by means of the PSD graphs given as insets in each AFM scan in Fig. 6.

The analysis of the MR curves reveals similar magnetic behavior for all the magnetic metals as a function of the film thickness. Clearly most of the MR curves are typical hard magnetization axis loops without the opening in the middle. Thus, the magnetization process is reversible and the magnetization rotates coherently in the applied magnetic field. The saturation field H_s decreases and the slope of the MR curve becomes steeper with the film thickness. The detailed $H_s(t)$ dependencies are discussed in more detail later in the text (see also Fig. 8). Note that the kinks in the MR loops are of optical origin only and usually appear if the polarization axis is slightly misaligned with respect to the sample plane.

On the one hand, for all three wedges a closed coverage of the ripple template is visible in the AFM images at thicknesses below a few nanometers. This is despite the fact that the surface energy for SiO_2 ($\sigma < 0.5$ J/m^2) is even lower than for metals. On the other hand, 3D island growth is visible in the AFM images for larger thicknesses of Py [Fig. 6(a)] and Co [Fig. 6(b)]. In the case of thick Fe an even more complicated growth microstructure is found [Fig. 6(c)].

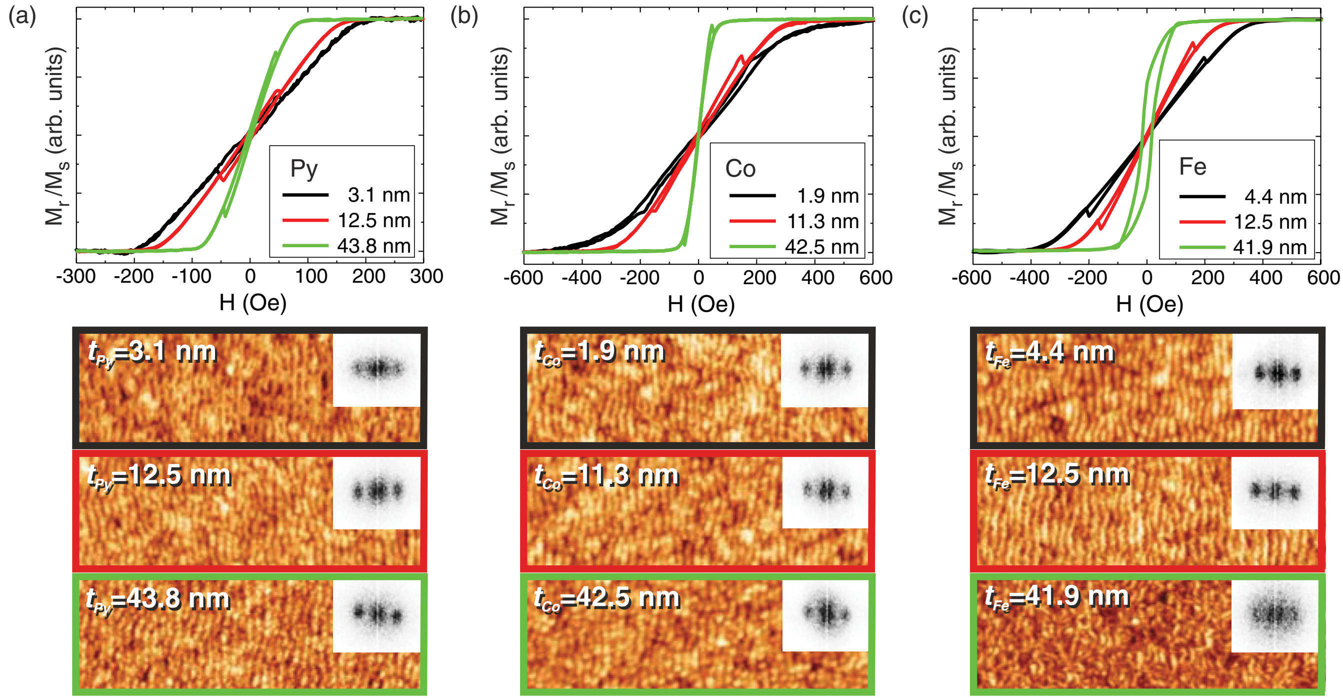

FIG. 6. (Color online) Magnetization reversal loops taken for different film thicknesses (upper panels) and corresponding AFM images with PSD insets (lower panels) for the three materials (a) Py, (b) Co, and (c) Fe.

Except for the 41.9 nm Fe film, the lateral coherence of the ripple formation is conserved for the other films throughout the whole thickness as it is confirmed by the PSD spectra (insets in each AFM graph in Fig. 6). The Fourier satellites peaks that correspond to the ripple wavelength are easily distinguishable from the background and have a strong anisotropic symmetry, slightly diminished for the maximum thickness. The PSD spectrum for the thickest Fe is more isotropic and the satellite peaks are hardly visible, which is the consequence of the overgrowth microstructure interconnecting ripple crests. In addition, the MR loop from this Fe thickness region has a clearly visible opening suggesting a nucleation of magnetic domains along the hard axis direction rather than the coherent magnetization rotation only.

Vaz *et al.*[33] proposed a model for the magnetization profile as a function of the film thickness for coherent interfaces [see Figs. 7(a) and 7(b)]. Two thickness regimes were distinguished: (i) Low thicknesses, where the magnetization follows the roughness profile. Thus, the magnetostatic energy is reduced due to "orange-peel" effects [Fig. 7(a)]. (ii) Large thicknesses, where the linear increase of exchange and anisotropy energy brings the system to the uniform magnetic state, e.g., dipolar charges act as a surface anisotropy contribution that is superimposed on the volume contributions [Fig. 7(b)].

However, the model is not fully appropriate for nonideal systems like our polycrystalline rippled films, where the tilt of the magnetization can be nonuniform over the film thickness. Thus, micromagnetic simulations have been performed in order to explain certain inconsistencies between the Vaz *et al.* model and our experimental findings, i.e., clearly visible dipolar contributions even for small magnetic metal thicknesses [see Figs. 7(c) and 8].[34]

The simulations were performed for rippled Fe films with various thicknesses in the range of 1–20 nm. Neither uniaxial nor cubic anisotropy contributions were taken into account. In order to obtain an alignment of the magnetization in the x–z plane [perpendicular to the ripple crests; see inset of Fig. 7(e)] a 100 nm thick stripe was simulated that was periodically extended along the x direction. The simulation cell size was $0.2 \times 10 \times 0.1$ nm^3. The ripple wavelength and peak-to-peak amplitude were set to $\lambda = 25$ nm and $h = 2$ nm, respectively. Data from the x–z planes were averaged over all slices along the y direction. Note that the simplified ripple model in the simulation assumes perfectly aligned and extended ripples. It does not take the ripple dislocations and imperfections into account. Hence, especially for very thin films this might lead to deviations from the experiment.

From the simulations depicted in Figs. 7(c) and 7(d) for a thin (2 nm) and thick (20 nm) Fe layer, roughness induced magnetic dipolar stray fields were obtained. In contrast to the model of Vaz *et al.* the dipolar fields also occur for very small film thicknesses indicating a deviation of the magnetization alignment with respect to the surface corrugation. However, the dipolar field strength at the thin film thickness regime [Fig. 7(c)] is one order of magnitude smaller than for the thick film thickness regime [Fig. 7(d)]. Furthermore, these fields are nonuniform over the Fe film thickness, which leads to a thickness dependent magnetization tilt in the regime of large layer thicknesses. Starting at the surface the tilt of $\vec{m}$ decreases with increasing depth until it reaches its smallest tilt in the middle of the layer. Hence a nonuniform magnetization distribution with respect to thickness is obtained. For thin thicknesses this observation is less pronounced since the dipolar field is not mainly located at the surface anymore but penetrates nearly uniformly the whole layer.

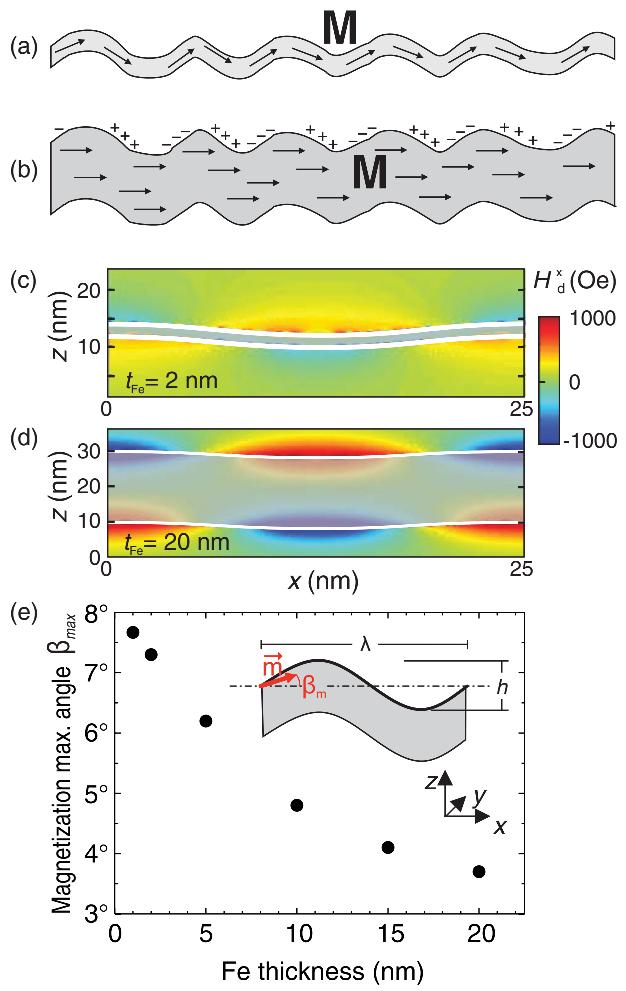

FIG. 7. (Color online) Simplified sketch of the magnetization orientation along the hard axis for (a) thin and (b) thick rippled ferromagnetic layers. Dipolar charges contribute to the anisotropy energy for thicker samples only (b). (c) Micromagnetic simulations for the thin and (d) thick Fe layer (gray shaded area) displaying the x component of the roughness induced dipolar stray field. (e) Shows the Fe thickness dependence of the magnetization's maximum tilt angle $\beta_{\max}$ from the x direction (geometry displayed in inset), obtained from the simulations.

To extract the influence of the layer thickness on the magnetization tilt we have calculated the local tilt angle β of the magnetization, counted from the x direction [see inset in Fig. 7(e)]. Since β varies with the local surface modulation and even within the film we used the maximum value $\beta_{\max}$ to characterize the behavior. For a film perfectly following the surface corrugation like sketched in Fig. 7(a) $\beta_{\max}$ should be 14.1° for the ripple geometry used. Figure 7(e) shows the calculated dependence of $\beta_{\max}$ as a function of the Fe thickness. One can see that the magnetization vector tilts in direction of the ripple curvature, however, due to exchange interaction and shape anisotropy in the film plane this tilt is not complete but slightly larger than 50% of the expected maximum of 14.1° for ideal films. $\beta_{\max}$ clearly decreases as a function of the film thickness, marking the fading influence of the surface towards bulklike behavior. Thus the amount of dipolar charges in the thin film thickness regime [refer to Figs. 8(a)–8(c)] will be relatively smaller compared to the thick film regime due to combination of a larger $\beta_{\max}$ and possible discontinuities of the film.

Nevertheless, our simulations clearly show that the magnetization vector oscillates with the surface modulation but never follows perfectly the corrugation. The latter finally leads to dipolar stray fields and an inhomogeneous magnetization distribution over the layer thickness in the thick layer regime.

Indeed, the linearized thickness dependence of the MOKE saturation field H_s shown in Figs. 8(a)–8(c) for all three metals clearly reveals those two magnetization regions. The solid and dashed lines are linear fits to the two thickness regimes. There is no gradual transition between the two regions but a kink. In the hard-axis configuration, i.e., perpendicularly to the ripple crests, the UMA can be written as $H_s = 2K_{2\|}/M_s$. In addition, H_s can be separated into a volume contribution H_s^V, and two surface/interface contributions H_s^S according to

$$H_s = H_s^V + 2\frac{H_s^S}{t}. \tag{4}$$

The resulting fit parameters H_s^V and H_s^S for the thin film region (I) and thick film region (II) of the wedge are listed in Table II.

In the thin film range H_s^S is less than a few percent of H_s^V. In region II it is the opposite effect, i.e., H_s^S is much larger. As we relate surface contributions of the UMA purely to dipolar interactions, i.e., stray field charges, we can conclude that for the thin film regime they are basically negligible, i.e., H_s^S is close to zero or negative, whereas volume contributions become important. The negative sign of the surface contribution H_s^S in the thin film region is puzzling. In general it might indicate that an in-plane spin reorientation transition between the thin and thick film thickness regime takes place. Thus, H_s^S and H_s^V favor orthogonal alignment, i.e., H_s^S is aligned perpendicular to the ripple crests, whereas H_s^V is oriented along them. This might be caused by the ripple dislocations in combination with thin films giving rise to a broken symmetry. The volume contribution H_s^V, on the other hand, is often related to the lattice strain[35] that in general is higher for the thin films than for the thick ones. The existence of two distinguishable regimes is nicely reflected by our data and it is in agreement with the micromagnetic simulations considering a smaller amount of dipolar charges for the thin film regime. The critical thickness t_{crit} can be extracted from the $tH_s(t)$ dependencies [see Fig. 8(a)–8(c)]. It is about 7 nm for Fe and Co, and about 12 nm for Py, respectively.

TABLE II. Volume and surface contributions to the UMA taken from the fits to the thin and thick film regime, i.e., below and above the critical thickness.

	Thin film (region I)		Thick film (region II)	
Material	H_s^V (Oe)	H_s^S (Oe)	H_s^V (Oe)	H_s^S (Oe)
Py	217.9	3.1	53.5	923.5
Co	588.9	– 19.4	21.8	1870.6
Fe	485.1	– 45.4	117.9	1300.4

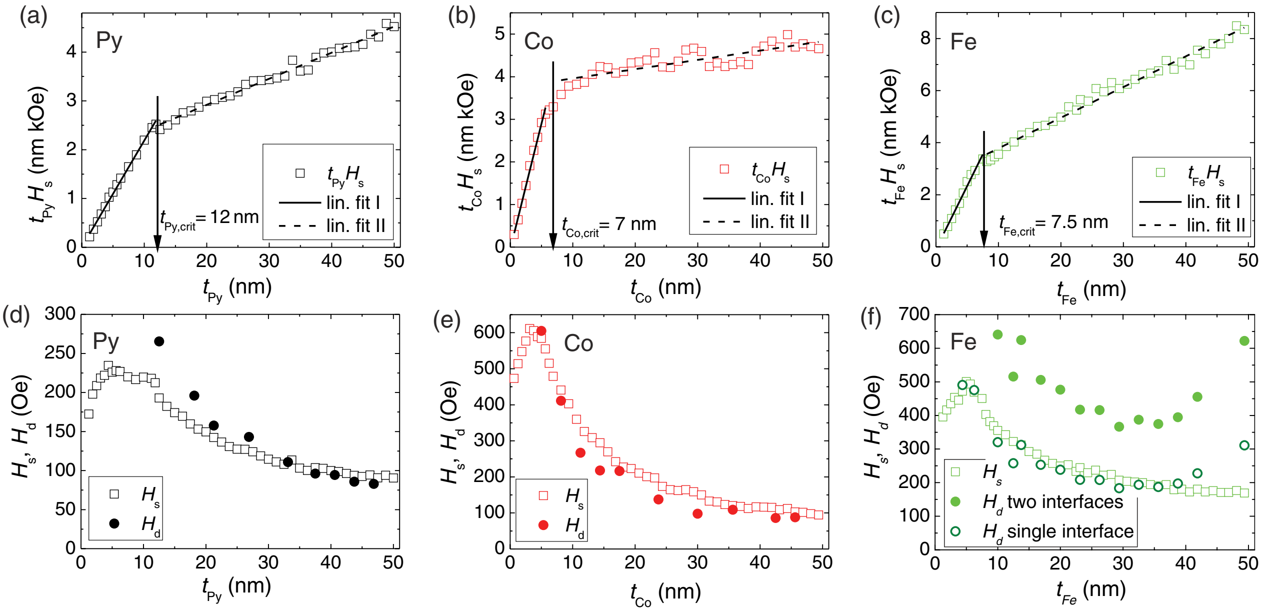

FIG. 8. (Color online) (a)–(c) Thickness dependencies of $t\,H_s$ for the three different materials on 25 nm ripples, respectively. Arrows denote the critical thickness between the two linear fit ranges (solid and dashed lines). (d)–(f) Corresponding thickness dependencies of H_s and H_d.

In Figs. 8(d)–8(f) the $H_s(t)$ data (open symbols) is given and compared with the theory of demagnetizing fields due to surface roughness by Schlömann.[36] For a periodic ripple profile with rms roughness ω_{rms} and wavelength λ the formula for the uniaxial in-plane anisotropy field can be written as follows:[16,36]

$$H_d = 4\pi M_s \frac{2\pi\omega_{rms}^2}{\lambda t}. \qquad (5)$$

All parameters in Eq. (5) are acquired experimentally except M_s, where the bulk values were taken from literature. ω_{rms} and λ are obtained from the AFM scans and t is obtained from quartz thickness monitoring during deposition. The interface factor 2 from the numerator accounts for the number of interfaces in our system, i.e., (i) the bottom ripple SiO_2/magnetic metal and (ii) the top magnetic metal/cup layer interface. The results are shown as solid symbols. For Py and Co we obtain a good agreement between the experiment (H_s) and theory (H_d) that clearly indicates the origins of the UMA are the dipolar interactions due to surface modulations [see Fig. 7(b)]. For Fe only a qualitative agreement of the functional trend is obtained. Lower H_s values suggest smaller M_s than the literature bulk value used. As mentioned already, from SQUID measurements on this particular sample we obtained $4\pi M_s \approx 15$ kG only. This might be possible while assuming no texture in our Fe films (that in general would enhance the anisotropy as well as the magnetization). Due to the cubic crystalline anisotropy of Fe and its strong 3D island film growth, M_s is expected to be lower than for bulk. Thus, a smaller $4\pi M_s$ of $\approx$12.3 kG would bring our experimental data and the theory to good agreement. However, it is hard to believe that for any reason M_s would drop by half compared to the bulk value. Surprisingly, removing the factor 2 from Eq. (5)—that in fact corresponds to a system with a single rippled (bottom only) interface—brings the model and experiment perfectly together, without the need to change M_s [see the open circles in Fig. 8(f)]. The influence of the top interface might be neglected in the calculation if the interface is stochastically rough and nonrippled. This is likely not a completely true picture, and it might be necessary to account for the noncoherent Fe growth on rippled SiO_2 as visible in Fig. 6(c), where the ripple profile is hardly visible for larger Fe thicknesses. Most probably both effects should be considered together, namely a lower M_s due to absence of texture in Fe, and a noninteger value (in the range of 1–2) of the interface factor from Eq. (5). In addition, the rapid increase of H_d for Fe thicknesses larger than 40 nm results from the increased roughness and diminishing of the lateral coherence of the ripples [cf. Fig. 6(c)]. As explained earlier this is due to the microstructural overgrowth in between ripple crests. Nevertheless, considering the simplicity of the theoretical model the agreement between the experiment and the theory is still intriguing.

IV. CONCLUSION

Periodically modulated surfaces can be used as a template for magnetic thin films to induce uniaxial magnetic anisotropy along the ripple crest direction. From the thickness dependence we find two characteristic regions where the uniaxial surface and volume contributions change their role. As a consequence of competing surface and volume contributions an in-plane spin reorientation transition at the critical thickness takes place. In the low thickness range of a few nanometers the uniaxial volume anisotropy is important as the magnetization tries to follow the surface corrugation. Above this critical thickness dipolar stray fields from the surface determine the uniaxial anisotropy. Our micromagnetic simulations qualitatively support experimental findings with respect to the relative strength of the dipolar stray fields generated due to the ripple surface morphology between the thin and thick film thickness regime that elucidates origins of the UMA in our magnetic patterned systems. Moreover, they show that the magnetization vector tilts in direction of the surface modulation but never follows perfectly the surface morphology.

ACKNOWLEDGMENTS

E.Č. appreciates the financial support from SAS Centre of Excellence: CFNT MVEP. This work is supported by the Deutsche Forschungsgemeinschaft (Grant No. FA314/6-1) and partially by EuroMagNET (EU Contract No. 228043).

---

[*] Corresponding author: m.liedke@hzdr.de; Present address: Institute of Radiation Physics, Helmholtz-Zentrum Dresden-Rossendorf, P.O. Box 510119, 01314 Dresden, Germany.

[†] Present address: Facilitation Centre for Industrial Plasma Technologies, Institute for Plasma Research, A-10/B, G.I.D.C. Electronics Estate, Sector 25, Gandhinagar - 382044, Gujarat, India.

[‡] Present address: Institute of Physics, Faculty of Science, P.J. Šafárik University, 041 54 Košice, Slovakia.

[1] M. V. R. Murty, Surf. Sci. **500**, 523 (2002).

[2] M. A. Makeev, R. Cuerno, and A.-L. Barabási, Nucl. Instrum. Methods Phys. Res. Sect. B **197**, 185 (2002).

[3] W. L. Chan and E. Chason, J. Appl. Phys. **101**, 121301 (2007).

[4] J. Fassbender, T. Strache, M. O. Liedke, D. Markó, S. Wintz, K. Lenz, A. Keller, S. Facsko, I. Mönch, and J. McCord, New J. Phys. **11**, 125002 (2009).

[5] M. Navez, C. Sella, and D. Chaperot, C. R. Hebd. Seances Acad. Sci. **254**, 240 (1962).

[6] R. M. Bradley and J. M. E. Harper, J. Vac. Sci. Technol. A **6**, 2390 (1988).

[7] P. Sigmund, J. Mater. Sci. **8**, 1545 (1973).

[8] A. Keller and S. Facsko, Materials **3**, 4811 (2010).

[9] J. Muñoz García, M. Castro, and R. Cuerno, Phys. Rev. Lett. **96**, 086101 (2006).

[10] F. Bisio, R. Moroni, F. B. de Mongeot, M. Canepa, and L. Mattera, Appl. Phys. Lett. **89**, 052507 (2006).

[11] F. Bisio, R. Moroni, F. B. de Mongeot, M. Canepa, and L. Mattera, Phys. Rev. Lett. **96**, 057204 (2006).

[12] R. Moroni, F. Bisio, F. B. de Mongeot, C. Boragno, and L. Mattera, Phys. Rev. B **76**, 214423 (2007).

[13] D. Sekiba, R. Moroni, G. Gonella, F. B. de Mongeot, C. Boragno, L. Mattera, and U. Valbusa, Appl. Phys. Lett. **84**, 762 (2004).

[14] K. Zhang, F. Rotter, M. Uhrmacher, C. Ronning, J. Krauser, and H. Hofsäss, New J. Phys. **9**, 29 (2007).

[15] K. Zhang, M. Uhrmacher, H. Hofsäss, and J. Krauser, J. Appl. Phys. **103**, 083507 (2008).

[16] M. O. Liedke, B. Liedke, A. Keller, B. Hillebrands, A. Mücklich, S. Facsko, and J. Fassbender, Phys. Rev. B **75**, 220407 (2007).

[17] M. Körner, K. Lenz, M. O. Liedke, T. Strache, A. Mücklich, A. Keller, S. Facsko, and J. Fassbender, Phys. Rev. B **80**, 214401 (2009).

[18] A. Keller, L. Peverini, J. Grenzer, G. J. Kovacs, A. Mücklich, and S. Facsko, Phys. Rev. B **84**, 035423 (2011).

[19] K. V. Sarathlal, D. Kumar, and A. Gupta, Appl. Phys. Lett. **98**, 123111 (2011).

[20] M. O. Liedke, M. Körner, K. Lenz, F. Grossmann, S. Facsko, and J. Fassbender, Appl. Phys. Lett. **100**, 242405 (2012).

[21] A. Berger, U. Linke, and H. P. Oepen, Phys. Rev. Lett. **68**, 839 (1992).

[22] C. Boeglin, S. Stanescu, J. P. Deville, P. Ohresser, and N. B. Brookes, Phys. Rev. B **66**, 014439 (2002).

[23] M. J. Carey, J. R. Childress, and S. Maat, US Patent No. 7,529,066 (5 May 2009).

[24] M. J. Carey, J. R. Childress, E. E. Fullerton, and S. Maat, US Patent No. 7,360,300 (22 April 2008).

[25] C. Teichert, J. Barthel, H. P. Oepen, and J. Kirschner, Appl. Phys. Lett. **74**, 588 (1999).

[26] B. Borca, O. Fruchart, P. David, A. Rousseau, and C. Meyer, Appl. Phys. Lett. **90**, 142507 (2007).

[27] Y. Park, E. E. Fullerton, and S. D. Bader, Appl. Phys. Lett. **66**, 2140 (1995).

[28] A. Keller, S. Roßbach, S. Facsko, and W. Möller, Nanotechnology **19**, 135303 (2008).

[29] A. Biermanns, U. Pietsch, J. Grenzer, A. Hanisch, S. Facsko, G. Carbone, and T. H. Metzger, J. Appl. Phys. **104**, 044312 (2008).

[30] I. Horcas, R. Fernandez, J. M. Gomez-Rodriguez, J. Colchero, J. Gomez-Herrero, and A. M. Baro, Rev. Sci. Instrum. **78**, 013705 (2007).

[31] B. Ziberi, F. Frost, T. Höche, and B. Rauschenbach, Phys. Rev. B **72**, 235310 (2005).

[32] J. Lindner, I. Barsukov, C. Raeder, C. Hassel, O. Posth, R. Meckenstock, P. Landeros, and D. L. Mills, Phys. Rev. B **80**, 224421 (2009).

[33] C. A. F. Vaz, S. J. Steinmüller, and J. A. C. Bland, Phys. Rev. B **75**, 132402 (2007).

[34] M. R. Scheinfein, http://llgmicro.home.mindspring.com

[35] S. Blundell, *Magnetism in Condensed Matter* (Oxford University Press, New York, 2011).

[36] E. Schlömann, J. Appl. Phys. **41**, 1617 (1970).